HOMOGENIZATION-BASED SPACE-TIME TOPOLOGY OPTIMIZATION OF TUNABLE MICROSTRUCTURES

A.F. Keleş, İ. Temizer, & *M. Cakmakci*

Department of Mechanical Engineering, Bilkent University, Ankara, Turkey

*Address all correspondence to: İ. Temizer, Department of Mechanical Engineering, Bilkent University, 06800 Ankara, Turkey, E-mail: temizer@bilkent.edu.tr

A topology optimization framework is developed for smart materials with tunable microstructures. The framework addresses spatial and temporal design variables in a unified setting so as to deliver the optimal periodic microstructure with stimulus-sensitive constituents. The optimal topology allows the macroscopic response of the microstructure to track a time-dependent cyclic path in the stress–strain space with minimal error. The relevant homogenization-based variational analysis for the sensitivity-based optimization framework incorporates not only material variables but also the geometry information regarding the unit cell. Extensive numerical investigations demonstrate the ability of the developed approach to deliver optimal topologies for realizable target macroscopic paths. The error in optimization increases monotonically with the degree of unrealizability, yet the critical role of the microstructure in minimizing the error in comparison to a pure time optimization approach is demonstrated in all cases.

KEY WORDS: *space–time topology optimization, homogenization, tunable microstructures, smart materials, programmable composites*

1. INTRODUCTION

Topology optimization is a well-established methodology for designing microstructured materials. Starting with the pioneering homogenization-based approach in Bensøe and Kikuchi (1988), advances in computational frameworks (Wu et al., 2021) in combination with novel manufacturing techniques (Liu et al., 2018) have enabled the practical application of this methodology in a broad range of settings. Because conventional optimal microstructure designs are typically targeted for a specific objective, their static nature does not allow them to adapt to time-varying demands. The ability of the macroscopic response to follow such demands so as to deliver improved response at all times can be important and is exemplified in the application of morphing materials (Kuder et al., 2013; Wenz et al., 2021) and novel actuators (Kallio et al., 2007; Li et al., 2014) among others. In general, this might be achieved by extending microstructural analysis and design toward macroscopic tunability.

Tunability might be achieved by allowing the microstructure to respond to an external stimuli, such as thermal (Cai et al., 2021; Restrepo et al., 2016a) and magnetic (Jackson et al., 2018; Li et al., 2010) fields, as well as electrical (Kuder et al., 2013; Shan et al., 2015), fluidic (Zhang et al., 2018), electrochemical (Xia et al., 2019), and light (Gump et al., 2004) excitation. Essentially relying on the existence of multiple phases with varying degrees of sensitivity to the stimuli, the programmable behavior that such smart materials display cannot be achieved without the critical role of the microstructure (Cai et al., 2021). In many of these cases, notably for magnetorheological materials (Kallio et al., 2007), the macroscopic response is continuously variable in a controllable manner based on the stimulus signal. In the case of predefined programming, for instance through deformation (Clausen et al., 2015) and multiple stages of buckling (Haghpanah et al., 2016b; Rafsanjani et al., 2015) or through mechanistic on–off approaches (Haghpanah et al., 2016a), continuity and controllability are limited yet the approach still offers a degree of flexibility that cannot be achieved by conventional materials or by metamaterials with static properties (Lee et al., 2012).

The analysis of the type of the previously tunable microstructures summarized can be carried out via approximate approaches, in particular, for trusslike morphologies (Wenz et al., 2021; Zhang et al., 2018), or through a more detailed numerical approach in the presence of significant nonlinearities (Rafsanjani et al., 2015; Restrepo et al., 2016b). However, an inverse study that addresses material design within a general topology optimization framework so as to achieve a target smart response in an optimal fashion without any restriction on the microstructural features is lacking in the literature.

The goal of the present study is to present such a framework in the context of homogenization. Within this framework, the focus is on both spatial optimization with respect to the microstructural geometry as well as on temporal optimization with respect to the tunability of the constituents. The resulting optimization framework treats the topology in space and time in a unified setting and aims to identify the microstructure that has stimulus-responsive constituents distributed to attain a target time-varying macroscopic response with minimal error. On the basis of the study in Özcan et al. (2020), which forms a foundation for the present work, the motivation for this approach is twofold. Firstly, the ability to realize the target macroscopic smart response critically relies on the microstructure. As a consequence, significant error may be observed if the stimulus-sensitive microscopic phases are distributed in an *a priori* prescribed morphology and one seeks to determine the external signals that should be delivered to them toward optimal tracking of the target response, which is a pure time optimization problem. Secondly, even when the target smart response is realizable for the prescribed microstructure, the practical identification of how the external signals should vary over time to minimize the tracking error relies on control theory. An implementation based on control theory is essential in the application of smart materials in the presence of uncertainties but is computationally inefficient for assessing the optimality of candidate microstructures for minimal error. The space–time topology optimization framework to be developed will circumvent both of these difficulties.

In realizing this goal, the emphasis will be on the optimization framework without an explicit formulation of the constitutive link between the external stimulus and the microscopic response. At most, two stimulus-responsive phases will be admitted and their response will be limited to elasticity at all times. It is anticipated that the developed framework is a first step toward the incorporation of detailed models for the constitutive response. On the other hand, in view of the central role of the spatial topology, the optimization of the periodic material distribution will be realized within a unit cell geometry, which will simultaneously evolve toward the optimal configuration. This offers an additional degree of freedom in optimization, the importance of which is often overlooked.

In order to address the stated goals, the variational analysis of the design framework will first be provided, starting with a brief statement of the homogenization problem that is followed by a sensitivity analysis with respect to material and geometry variables. Next, the tunable features of the microstructure will be introduced and the unified space–time optimization framework is discussed. Extensive numerical investigations will first highlight the importance of geometry optimization as well as the critical role of the microstructure in ensuring the optimal reflection of tunability toward the macroscopic response. Target responses range from realizable cyclic paths in the macroscopic stress–strain space to unrealizable ones where the combined space–time approach will nevertheless perform significantly better than a pure time optimization approach on predefined microstructures. The practical application of the resulting designs within a control implementation will additionally be addressed, and the study will be concluded with a discussion of the capabilities and future extensions that are offered.

2. VARIATIONAL DESIGN ANALYSIS

2.1 Homogenization Problem

A periodic composite is considered with a unit cell $\mathcal{Y}$ that is assigned a position vector $\boldsymbol{y}$. Assuming a linearly elastic microscopic response $\boldsymbol{\sigma} = \mathbb{E}\boldsymbol{\epsilon}$ that remains so at all times, the microstructure topology in $\mathcal{Y}$ is associated with a time-dependent elasticity tensor distribution $\mathbb{E}(\boldsymbol{y}, t)$. Indicating averaging for a generic variable $\mathcal{Q}$ over $\mathcal{Y}$ through the notation $\langle \mathcal{Q} \rangle = |\mathcal{Y}|^{-1} \int_{\mathcal{Y}} \mathcal{Q} \, dv$, the macroscopic response is characterized by the tensor $\overline{\mathbb{E}}(t)$, which relates average stress and strain at a given time, as follows:

$$\bar{\boldsymbol{\sigma}} = \langle \boldsymbol{\sigma} \rangle \tag{1a}$$

$$\bar{\boldsymbol{\epsilon}} = \langle \boldsymbol{\epsilon} \rangle \tag{1b}$$

$$\bar{\boldsymbol{\sigma}} = \overline{\mathbb{E}}\bar{\boldsymbol{\epsilon}} \tag{1c}$$

where the stress field is such that it induces anti-periodic tractions on $\partial \mathcal{Y}$, whereas the strain field is associated with periodic displacements. Noting that $\mathbb{E}$ displays appropriate minor and major symmetries with respect to its indices, the components of $\overline{\mathbb{E}}$ are then determined through the following classical expression (Sanchez-Palencia, 1980):

$$\Gamma_{pq}^{kl} = \delta_{kp}\delta_{lq} + \Lambda_{pq}^{kl} \tag{2a}$$

$$\overline{\mathbb{E}}_{ijkl} = \left\langle \mathbb{E}_{ijpq}\,\Gamma_{pq}^{kl} \right\rangle \tag{2b}$$

where δ_{ij} is the Kronecker delta. The tensor $\boldsymbol{\Lambda}^{kl} = \nabla \boldsymbol{\lambda}^{kl}$ is associated with the periodic vector field $\boldsymbol{\lambda}^{kl}(\boldsymbol{y}, t)$, which satisfies the cell problem

$$\frac{\partial}{\partial y_j}\left(\mathbb{E}_{ijpq}\,\Gamma_{pq}^{kl} \right) = 0 \tag{3}$$

that ensures the symmetry of $\boldsymbol{\lambda}^{kl}$ with respect to k and l so that $\overline{\mathbb{E}}$ clearly displays minor symmetries.

2.2 Material Variable Sensitivity

Within a design problem, $\mathbb{E}(\boldsymbol{y}, t)$ depends on a set of material variables that parametrize its distribution. Indicating a prescribed functional relation to a generic material variable ζ through the notation $\mathbb{E}[\zeta]$, Eqs. (2a) and (2b) implicitly implies a macroscopic parametrization $\overline{\mathbb{E}}[\zeta]$. The sensitivity expression $\partial \overline{\mathbb{E}}_{ijkl}/\partial \zeta$ that will be required within a numerical optimization scheme is typically derived through the adjoint method (Bendsøe and Sigmund, 2004). Here, a compact variational formulation is briefly noted. To this end, note that the direct evaluation of the sensitivity via Eq. (2b) requires calculating the term $\partial \Lambda_{pq}^{kl}/\partial \zeta$ by employing the sensitivity of Eq. (3), which is unfavorable in view of the large number of variables. To avoid its appearance, the weak form of the cell problem (3) is constructed by introducing a periodic vector field $\boldsymbol{\eta}$, as follows:

$$\left\langle \frac{\partial \eta_p}{\partial y_q}\,\mathbb{E}_{pqrs}\,\Gamma_{rs}^{kl} \right\rangle = 0 \tag{4}$$

Upon choosing $\boldsymbol{\eta}$ as $\boldsymbol{\lambda}^{ij}$ and $\partial \boldsymbol{\lambda}^{ij}/\partial \zeta$, respectively, the weak form implies the relations

$$\left\langle \Lambda_{pq}^{ij}\,\mathbb{E}_{pqrs}\,\Gamma_{rs}^{kl} \right\rangle = 0, \qquad \left\langle \frac{\partial \Lambda_{pq}^{ij}}{\partial \zeta}\,\mathbb{E}_{pqrs}\,\Gamma_{rs}^{kl} \right\rangle = 0 \tag{5}$$

When the first vanishing average is added to Eq. (2b), one obtains the following alternative expression:

$$\overline{\mathbb{E}}_{ijkl} = \left\langle \Gamma_{pq}^{ij}\,\mathbb{E}_{pqrs}\,\Gamma_{rs}^{kl} \right\rangle \tag{6}$$

that also clarifies the major symmetry of $\overline{\mathbb{E}}$ with respect to its indices. Upon invoking the second vanishing average together with this symmetry and recalling Eq. (2a), the sensitivity of Eq. (6) now takes the following practical form:

$$\frac{\partial \overline{\mathbb{E}}_{ijkl}}{\partial \zeta} = \left\langle \Gamma_{pq}^{ij}\,\frac{\partial \mathbb{E}_{pqrs}}{\partial \zeta}\,\Gamma_{rs}^{kl} \right\rangle \tag{7}$$

In view of the variational structure of the finite element method, this form delivers an exact sensitivity at arbitrary mesh resolutions.

2.3 Geometry Variable Sensitivity

A fixed unit cell geometry, such as a cube, can restrict the design space and therefore lead to an arrest of the microstructure development during topology optimization (Çakal et al., 2019). Periodicity allows one to define the nonunique but smallest possible [i.e., primitive (Ashcroft and Mermin, 1976)] unit cell as a parallelepiped. Therefore, full flexibility can be assigned to the unit cell geometry by constructing it through the linear transformation $\boldsymbol{y} = \boldsymbol{A}\boldsymbol{y}_o$ of a reference cube $\mathcal{Y}_o$ with position vector $\boldsymbol{y}_o$. Here, all components of the tensor $\boldsymbol{A}$ or only selected quantities that are associated with it can be incorporated into the optimization scheme in order to relax the objective further toward the extremum. Indicating such a generic geometric quantity with γ, the sensitivity of $\overline{\mathbb{E}}[\zeta; \gamma]$ with respect to this new design variable must be determined because the macroscopic elasticity tensor is now parametrically dependent on $\boldsymbol{A}$ as well. For this purpose, introducing the notation $\langle \mathcal{Q} \rangle_o = |\mathcal{Y}_o|^{-1} \int_{\mathcal{Y}_o} \mathcal{Q} \, dv_o$ and noting that $\langle \mathcal{Q} \rangle = \langle \mathcal{Q} \rangle_o$, the sensitivity of Eq. (6) with respect to γ may be stated as follows:

$$\frac{\partial \overline{\mathbb{E}}_{ijkl}}{\partial \gamma} = \frac{\partial}{\partial \gamma} \left\langle \Gamma_{pq}^{ij} \, \mathbb{E}_{pqrs} \, \Gamma_{rs}^{kl} \right\rangle_o = \left\langle \frac{\partial \Lambda_{pq}^{ij}}{\partial \gamma} \, \mathbb{E}_{pqrs} \, \Gamma_{rs}^{kl} \right\rangle_o + \left\langle \Gamma_{pq}^{ij} \, \mathbb{E}_{pqrs} \, \frac{\partial \Lambda_{rs}^{kl}}{\partial \gamma} \right\rangle_o \tag{8}$$

Additionally defining $\nabla_o = \partial/\partial \boldsymbol{y}_o$ and $\boldsymbol{B} = \boldsymbol{A}^{-1}$, one may write

$$\boldsymbol{\Upsilon}^{kl} = \nabla_o \boldsymbol{\lambda}^{kl}, \qquad \boldsymbol{\Lambda}^{kl} = \boldsymbol{\Upsilon}^{kl} \boldsymbol{B} \tag{9}$$

such that the first of the two similar terms within Eq. (8) takes the following form:

$$\left\langle \frac{\partial \Lambda_{pq}^{ij}}{\partial \gamma} \, \mathbb{E}_{pqrs} \, \Gamma_{rs}^{kl} \right\rangle_o = \frac{\partial B_{mq}}{\partial \gamma} \left\langle \Upsilon_{pm}^{ij} \, \mathbb{E}_{pqrs} \, \Gamma_{rs}^{kl} \right\rangle + \left\langle \frac{\partial}{\partial y_q} \left(\frac{\partial \lambda_p^{ij}}{\partial \gamma} \right) \mathbb{E}_{pqrs} \, \Gamma_{rs}^{kl} \right\rangle \tag{10}$$

The latter integral vanishes in view of Eq. (4) upon choosing $\boldsymbol{\eta}$ as $\partial \boldsymbol{\lambda}^{ij}/\partial \gamma$. Analyzing the remaining term within Eq. (8) in a similar manner and noting $\partial \boldsymbol{B}/\partial \gamma = -\boldsymbol{B}(\partial \boldsymbol{A}/\partial \gamma)\boldsymbol{B}$, one obtains the sensitivity expression

$$\frac{\partial \overline{\mathbb{E}}_{ijkl}}{\partial \gamma} = -\frac{\partial A_{mn}}{\partial \gamma} \left(B_{nq} \left\langle \Lambda_{pm}^{ij} \, \mathbb{E}_{pqrs} \, \Gamma_{rs}^{kl} \right\rangle + \left\langle \Gamma_{pq}^{ij} \, \mathbb{E}_{pqrs} \, \Lambda_{rm}^{kl} \right\rangle B_{ns} \right) \tag{11}$$

Similar to Eq. (7), this expression ensures an efficient sensitivity evaluation based on $\boldsymbol{\lambda}^{kl}$ alone. In this work, the entirety of $\boldsymbol{A}$ is subject to optimization, i.e., γ coincides with its components. Because the homogenization framework does not account for the absolute size of the unit cell, it will be found convenient to enforce $|\mathcal{Y}| = |\mathcal{Y}_o|$ through the isochoric deformation constraint $\det \boldsymbol{A} = 1$, the sensitivity of which can easily be evaluated through Jacobi's formula for optimization purposes.

The importance of the unit cell geometry is often overlooked, but this had already been recognized in the pioneering study of Bensøe and Kikuchi (1988). Despite the fact that the present approach was developed independently, a very recent review on topology optimization (Wu et al., 2021) summarizes a limited number of works involving some type of unit cell geometry relaxation and recognizes the study by Barbarosie and Toader (2014) as the only approach that allows full relaxation. The formulation in Barbarosie and Toader (2014) overlaps with the approach presented herein; although the sensitivity analysis, despite reaching the same expression, follows a different route. Because Barbarosie and Toader (2014) has been acknowledged only in a handful of studies and never invoked in any of these to the best of the authors' knowledge, it is anticipated that the alternative and significantly more compact sensitivity analysis pursued above will be of interest. Moreover, such unrestricted unit cell geometry optimization has not been applied in a three-dimensional setting, which will be carried in the numerical investigations.

3. TUNABLE MICROSTRUCTURE DESIGN

3.1 Space–Time Topology

The tunable composite will be subject to topology optimization at both temporal and spatial levels. Within a bimaterial setting, the microstructure is described through two elasticity tensors $\mathbb{E}^{(1)}$ and $\mathbb{E}^{(2)}$. Following recent approaches

(Ansari et al., 2018; Bou Matar et al., 2012; Palacios et al., 2022; Trainiti et al., 2019), tunability is introduced into the design framework by endowing each material with the ability to respond to a time-dependent external stimulus $\phi^{(\alpha)}(t)$. As in Ansari et al. (2018), Trainiti et al. (2019), and Özcan et al. (2020), instead of modeling the constitutive relation to the stimulus, the time-dependence of each $\mathbb{E}^{(\alpha)}$ is explicitly invoked through a material-specific temporal variable $\tau^{(\alpha)}(t) \in [0, 1]$ such that

$$\mathbb{E}^{(\alpha)}[\tau^{(\alpha)}] = \mathbb{E}^{(\alpha)}_{\min} + \left(\mathbb{E}^{(\alpha)}_{\max} - \mathbb{E}^{(\alpha)}_{\min}\right) \tau^{(\alpha)}(t) \tag{12}$$

The variable $\tau^{(\alpha)}(t)$ is associated with the temporal topology of the microstructure. The spatial topology is now introduced in a standard density-based setting through an additional material variable $\rho(\boldsymbol{y}) \in [0, 1]$ such that

$$\mathbb{E}[\rho, \tau^{(1)}, \tau^{(2)}] = \mathbb{E}^{(1)} + \left(\mathbb{E}^{(2)} - \mathbb{E}^{(1)}\right) \rho^{\eta}(\boldsymbol{y}) \tag{13}$$

where η is a fixed parameter. In order to embed a scale into the space–time variations of $\mathbb{E}$ and also to avoid possible discretization dependence that would hinder convergence of the topology with discretization refinement, $\tau^{(\alpha)}(t)$ and $\rho(\boldsymbol{y})$ are generally defined through the filtering of actual design variables $k^{(\alpha)}(t)$ and $s(\boldsymbol{y})$, respectively. Therefore, the space–time topology of the elasticity tensor will be denoted through $\mathbb{E}[s, k^{(1)}, k^{(2)}]$, leading to a similar parametrization of its macroscopic counterpart $\overline{\mathbb{E}}$. Within the numerical investigations, each $\mathbb{E}^{(\alpha)}$ will be associated with an isotropic response that is characterized by a Young's modulus $E^{(\alpha)}$ and a Poisson's ratio $\nu^{(\alpha)}$. The latter will be fixed at a value of 0.3 for simplicity throughout this work. Instead of invoking the space–time formulation of Eqs. (12) and (13) through $\mathbb{E}^{(\alpha)}$, they are now directly applied to the variable elastic properties with the modulus amplitude $\Delta E^{(\alpha)}$ and the limits

$$E^{(\alpha)}_{\min} = E^{(\alpha)}_o - \Delta E^{(\alpha)}, \qquad E^{(\alpha)}_{\max} = E^{(\alpha)}_o + \Delta E^{(\alpha)} \tag{14}$$

It is highlighted that the temporal variation $\mathbb{E}^{(\alpha)}(t)$ at each point of the designed microstructure is completely identified once the optimal $\tau^{(\alpha)}(t)$ is determined. At this point, the constitutive relation between $\mathbb{E}^{(\alpha)}$ and the external stimulus $\phi^{(\alpha)}$ may be inverted for each point in time to determine the physical variation $\phi^{(\alpha)}(t)$ that delivers the desired $\mathbb{E}^{(\alpha)}(t)$. Therefore, $\tau^{(\alpha)}$ solely serves as an intermediate variable, which enables the decoupling of the exact details of the constitutive relation from the optimization of the temporal variation $\mathbb{E}^{(\alpha)}(t)$.

3.2 Discrete Optimization

The time optimization framework will aim to determine the temporal topology $k^{(\alpha)}(t)$ so as to adapt $\overline{\mathbb{E}}$ to a time-varying target response. The space optimization framework, on the other hand, will introduce flexibility toward this goal by seeking the spatial topology $s(\boldsymbol{y})$ in a suitable unit cell geometry that is defined through $\boldsymbol{A}$, which will help accomplish this adaptation with minimal error. For any given $\{s, k^{(1)}, k^{(2)}; \boldsymbol{A}\}$, $\overline{\mathbb{E}}$ is determined via Eq. (6). Its sensitivity with respect to any of the material design variables s and $k^{(\alpha)}$ is delivered through Eq. (7) while Eq. (11) delivers its sensitivity with respect to the components of $\boldsymbol{A}$.

With respect to material design within a finite element framework, the microstructure is discretized with $N_m \times N_m$ linear elements, element $I \in \{1, 2, \ldots, N_m^2\}$ being assigned a spatial material design variable $s_I \in [0, 1]$. Similarly, restricting the temporal variations to periodic ones in view of the targeted problems, the period T will be discretized with N_t steps and each step is assigned a temporal material design variable $k_n^{(\alpha)} \in [0, 1]$ with $n \in \{1, 2, \ldots, N_t\}$. Indicating the set of discrete material design variables with $\boldsymbol{s}$ and $\boldsymbol{k}^{(\alpha)}$, their filtered counterparts are denoted as $\boldsymbol{\rho}$ and $\boldsymbol{\tau}^{(\alpha)}$, respectively. In this work, the exponential erode filter (Svanberg and Svärd, 2013) will be invoked for the spatial variables with $\eta = 3$ in Eq. (13). A linear filter (Svanberg and Svärd, 2013) is suitable for the temporal variables but these were found to require no filtering for the chosen temporal discretization. It is noted that, in addition to enforcing the periodicity of $\lambda^{kl}(\boldsymbol{y}, t)$ toward the solution of Eq. (3), filtering is carried out by enforcing the periodicity of the operation with respect to the unit cell geometry.

3.3 Optimization Problem

In this work, the optimization problem of interest focuses on the macroscopic constitutive response of the tunable composite under periodic loading. Specifically, strain-driven cyclic loading will be imposed on the unit cell with a steady-state periodic loop of the form

$$\overline{\epsilon}_{ij}(t) = m_{ij}^{\epsilon} - a_{ij}^{\epsilon} \sin\left(\frac{2\pi t}{T_{ij}^{\epsilon}}\right) \tag{15}$$

where m_{ij}^{ϵ} and a_{ij}^{ϵ} are the mean and amplitude for $\overline{\epsilon}_{ij}$ with period T_{ij}^{ϵ}. As a response to this loading, a stress response is targeted in a similar form with cyclic function cyc and a phase θ_{ij}:

$$\overline{\sigma}_{ij}^{*}(t) = m_{ij}^{\sigma} + a_{ij}^{\sigma} \operatorname{cyc}\left(\frac{2\pi t}{T_{ij}^{\sigma}} + \theta_{ij}\right) \tag{16}$$

Because the means, amplitudes, and periods do not necessarily allow the stress and strain to satisfy Eq. (1c) if $\overline{\mathbb{E}}$ is constant, adaptation is necessary even without a phase. At any stage of loading with a given set of design variables, the actual stress output $\bar{\sigma} = \overline{\mathbb{E}}[s, k^{(1)}, k^{(2)}; A] \, \bar{\epsilon}$ will not be able to perfectly track the target value and an error ϕ_{ij} is induced over a cycle for a single stress component. These errors define the total tracking error Φ over a period, as follows:

$$\phi_{ij}(t) = \left[\frac{1}{T_{ij}^{\epsilon}} \int_{t-T_{ij}^{\epsilon}}^{t} \left(\frac{\overline{\sigma}_{ij}(t) - \overline{\sigma}_{ij}^{*}(t)}{\overline{\sigma}_{ij}^{*}(t)}\right)^2 \mathrm{d}t\right]^{1/2}, \qquad \Phi(t) = \sum_{i,j} \phi_{ij}(t) \tag{17}$$

The space–time topology optimization framework seeks to minimize this error. In Özcan et al. (2020), this was realized within a control theory framework based on temporal variations alone, whereas topology optimization will be invoked presently. When only temporal material design variables are employed, the two approaches are similar but not identical. In the control theory setting, the controller regards $\tau^{(\alpha)}(t)$ within Eq. (12) as a signal and attempts to update it such that the tracking error is minimized. It is necessary to start with initial conditions and move toward the steady-state loading conditions that are represented through $\overline{\epsilon}_{ij}(t)$. As a consequence, a transient regime is observed. Moreover, even after the macroscopic strain starts following the steady-state loop, the controller requires multiple periods before $\tau^{(\alpha)}(t)$ variations converge to their steady-state variations that represent optimality with respect to the controller setup. This optimality condition is based on the minimization of not $\Phi(t)$ but rather the contribution $\overline{\sigma}_{ij} - \overline{\sigma}_{ij}^{*}$ to its integrand for each i and j.

In the present topology optimization framework, on the other hand, it is sufficient to employ the tracking error as the objective and attempt to minimize it. Because each optimization iteration is independent of time, the tracking error is evaluated directly over a steady-state loading period such that Φ is rendered independent of time, i.e., $t = T_{ij}^{\epsilon}$ within Eq. (17). Since the conditions of optimality differ, the converged $\tau^{(\alpha)}(t)$ signals will, in general, differ as well. However, if there exist signals that render $\overline{\sigma}_{ij}(t)$ exactly equal to $\overline{\sigma}_{ij}^{*}(t)$, then both approaches are able to capture them such that their respective objectives vanish, to within the limitations of the controller setup or the temporal design variable resolution. Such a case will be referred to as realizable. Conversely, when such signals do not exist, the targeted response $\overline{\sigma}_{ij}^{*}(t)$ is unrealizable and the two approaches will deliver increasingly different converged signals with an increasing degree of unrealizability. For any unrealizable target response, the spatial material design variables, in combination with the geometry design variables, will act as additional optimization degrees of freedom that will enhance the ability of the present framework to further reduce the tracking error. Hence, the overall topology optimization problem may be stated as follows:

$$\text{minimize } \Phi[s, k^{(1)}, k^{(2)}; \gamma], \text{ subject to } \chi(s) = 0 \text{ and } \left\{s_I \in [0, 1], k_n^{(1)} \in [0, 1], k_n^{(2)} \in [0, 1]\right\} \tag{18}$$

where, in addition to the last set of inequality constraints, an equality constraint χ is imposed indirectly on s through ρ to enforce a target volume fraction ρ^* that is associated with $\mathbb{E}^{(2)}$: $\chi = (\langle\rho\rangle - \rho^*)^2/(\rho^*)^2$. Enforcing additional

constraints on the remaining design variables was not found necessary. Optimization was carried out based on the method of moving asymptotes (Svanberg, 1987). For this purpose, recalling Eqs. (7) and (11), the sensitivity of Φ with respect to $\xi \in \{s, k^{(1)}, k^{(2)}; \gamma\}$ may be stated as follows:

$$\frac{\partial \phi_{ij}(t)}{\partial \xi} = \frac{1}{\phi_{ij} T_{ij}^\epsilon} \int_{t-T_{ij}^\epsilon}^{t} \left(\frac{\overline{\sigma}_{ij}(t) - \overline{\sigma}_{ij}^*(t)}{\overline{\sigma}_{ij}^*(t)} \right) \frac{\partial \overline{\mathbb{E}}_{ijkl}}{\partial \xi} \left(\frac{\overline{\epsilon}_{kl}(t)}{\overline{\sigma}_{ij}^*(t)} \right) dt, \qquad \frac{\partial \Phi(t)}{\partial \xi} = \sum_{i,j} \frac{\partial \phi_{ij}(t)}{\partial \xi} \qquad (19)$$

4. NUMERICAL INVESTIGATIONS

4.1 Unit Cell Geometry Optimization

In a first step, pure unit cell geometry optimization is carried out to highlight its importance and determine appropriate limits on the optimization space regarding A. For this purpose, two microstructures with square unit cells are constructed (Fig. 1), both with $\{E^{(1)}, E^{(2)}, \rho^*\} = \{3.6\,\text{MPa}, 108\,\text{MPa}, 0.45\}$ but one having the phases oriented along 0 deg (unrotated); whereas this angle is 20 deg and the unit cell is oriented accordingly (rotated) for the second microstructure. The macroscopic elasticity tensor for each case is calculated and prescribed as a target $\overline{\mathbb{E}}^*$ within the objective function $\|\overline{\mathbb{E}} - \overline{\mathbb{E}}^*\|^2 / \|\overline{\mathbb{E}}^*\|^2$. In order to assess the optimization quality, the remaining error in the objective function will be referenced through the percentage value. In all examples, $N_m = 40$ is chosen for space optimization (Section 3.2). For the unrotated case, optimization without geometry adaptation is sufficient and delivers the expected microstructure. However, the corresponding result for the rotated case is a typical output for a suboptimal microstructure that cannot develop freely due to fixed geometry constraints. It is emphasized that the chosen exponential erode filter for the spatial variables can induce sharper topologies with distinct phases in comparison to alternative choices, such as the linear filter. However, the results may also appear comparatively jagged and are more prone to developing isolated features. Presently, in all examples, the optimization results on a unit cell are presented without any postprocessing. It is noted that, in all microstructure figures, three unit cells per direction are employed for clarity.

In order to investigate the relaxation of the domain constraints (Fig. 2), first, the off-diagonal components of A are fixed to zero and only the diagonal values are allowed to vary in the range $[\lambda^{-1}, \lambda]$. Because off-diagonal components will eventually also be allowed, which will enable rotation of the domain, $\lambda = 1.7$ was found to provide sufficient flexibility. Presently, even this limited pure-stretch geometry adaptation enables optimal microstructure development
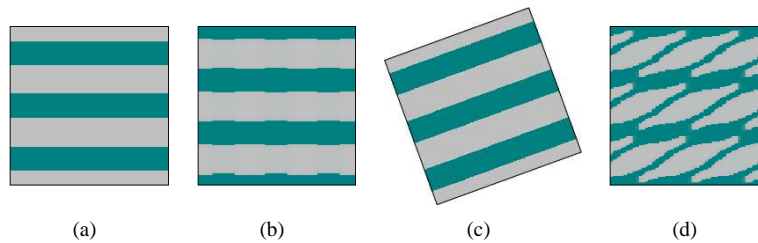

(a)	(b)	(c)	(d)

FIG. 1: A microstructure and its 20 deg rotated version are shown in (a) and (c). These are employed to generate target values $\overline{\mathbb{E}}^*$. In all figures, the gray and green phases are assigned $E^{(1)}$ and $E^{(2)}$, respectively. The optimization results on a fixed square domain are shown in (b) for the unrotated case and (d) for the 20 deg rotated case. Refer to the online version for color.
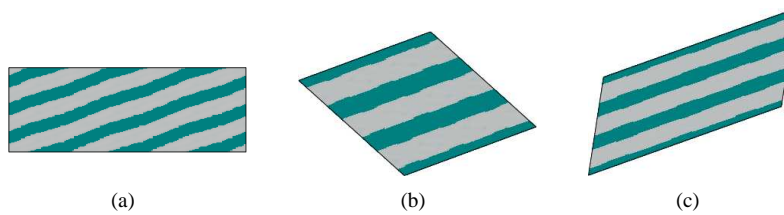

(a)	(b)	(c)

FIG. 2: Unit cell domain geometry optimization [(a) pure stretch, (b) pure rotation, and (c) full] is invoked for the target $\overline{\mathbb{E}}^*$ that is associated with the rotated microstructure in Fig. 1(c)

along a diagonal that closely matches 20 deg. Alternatively, pure-rotation geometry adaptation may be allowed by restraining the diagonal components to the range $[0.7, 1.0]$ and the off-diagonal ones to $[-0.8, 0.8]$, which offers sufficient flexibility for rotation through at least 45 deg. Higher rotations are implicitly captured through symmetry based on appropriate microstructure development. Once again, the expected microstructure develops freely. Finally, full freedom can be allowed in A where the diagonal component range is $[1/1.7, 1.7]$ and the off-diagonal range is $[-0.8, 0.8]$, also resulting in the optimal topology. The differences in the three optimal microstructures additionally highlight the nonunique choice of the unit cell.

For the preceding example, rotation naturally provides sufficient flexibility toward capturing the optimal design. As an alternative scenario, Fig. 3 shows two microstructures, based on the same Young's moduli as before and $\rho^* = 0.55$, one with a square geometry and a second that is obtained from the first through an isochoric linear map via 50% vertical stretch. When their elasticity tensors are prescribed as targets within the optimization scheme, the fixed square optimization domain successfully captures the first one but not the second, leaving isolated features that do not disappear with iterations and thereby increasing the optimization error. When pure-stretch adaptation of the domain is enabled, the error significantly diminishes and pure-rotation adaptation also delivers a comparable result (Fig. 4). To maintain sufficient generality toward cases where it may not be *a priori* clear as to which type of adaptation is sufficient, full flexibility in A will be maintained in the remaining investigations. Presently, this option also delivers a successful output, once again demonstrating the nonuniqueness in the choice of the unit cell.

It is highlighted that the objective error already decreases to the range of 10–20% even for the suboptimal microstructures of these examples, i.e., optimization delivers acceptable topologies. However, this value is an order of magnitude smaller at 1–3% when geometry optimization is enabled and can vanish at higher discretizations, thereby delivering better topologies not only qualitatively but also quantitatively. The advantage of geometry optimization lies in its ability to operate on a primitive unit cell. Relaxation of the topology development, which is reflected largely as a boundary effect, may alternatively be realized by employing increasingly larger supercells such that sufficient relaxation is attained internally (Çakal et al., 2019). However, this is a comparatively inefficient approach because it leads to considerably higher computational cost due to the increasing number of degrees of freedom for both the finite element calculations and the optimization step. In all subsequent examples, space optimization will include unit cell geometry optimization in addition to topology optimization within the adapted unit cell domain.

Finally, three-dimensional examples are provided in Fig. 5, based on the same Young's moduli as before and $\rho^* = 0.51$. In these examples, $N_m = 30$ is employed as the spatial resolution in view of the comparatively high
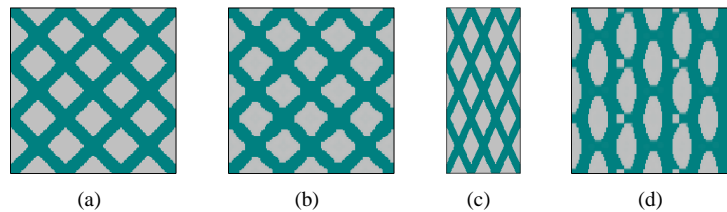

(a)   (b)   (c)   (d)

FIG. 3: A microstructure and its 50% stretched version are shown in (a) and (c). These are employed to generate target values $\overline{\mathbb{E}}^*$. The optimization results on a fixed square domain are shown in (b) for the unstreched case and (d) for the 50% streched case, respectively. The percentage values refer to the vertical stretch associated with the isochoric linear map.
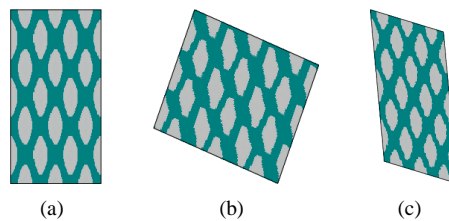

(a)   (b)   (c)

FIG. 4: Unit cell domain geometry optimization [(a) pure stretch, (b) pure rotation, and (c) full] is invoked for the target $\overline{\mathbb{E}}^*$ that is associated with the stretched microstructure in Fig. 3(c)
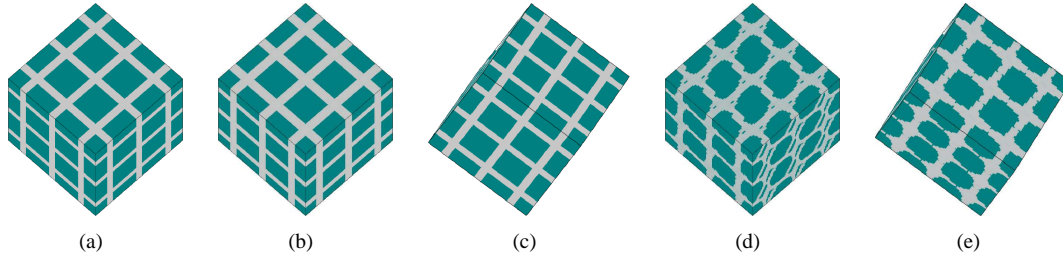
FIG. 5: A target microstructure ($\boldsymbol{A} = \boldsymbol{I}$) and its rotated version ($\boldsymbol{A} = \boldsymbol{A}_o$) are shown in (a) and (c). The corresponding optimization results on a fixed cubic domain are shown in (b) and (d), respectively. The result in (e) additionally invokes unrestricted unit cell geometry optimization for the target in (c). The edges of the fixed cubic domains define the coordinate system with respect to which remaining orientations may be assessed.

computational cost. When an untransformed ($\boldsymbol{A} = \boldsymbol{I}$) microstructure is targeted, optimization on a fixed cubic domain satisfactorily reconstructs the same topology with $< 3\%$ error in the objective. Subsequently, a transformed target microstructure is described through $\boldsymbol{A}_o = \boldsymbol{A}_3 \boldsymbol{A}_2 \boldsymbol{A}_1$, where $\boldsymbol{A}_i$ represents rotation about the y_i-axis through 20 deg. When optimization is carried out on a fixed cubic domain, an oriented microstructure attempts to develop unsatisfactorily with a resulting objective error of $> 13\%$. On the other hand, by allowing for unrestricted unit cell geometry optimization with the earlier noted limits on the entries of $\boldsymbol{A}$, a satisfactory topology development is once again observed with a corresponding objective error of $< 2\%$.

4.2 Space–Time Topology Optimization

In order to demonstrate the advantages of combined space–time topology optimization for tunable microstructures, only time optimization is first carried out on a prescribed microstructure. Because the stress–strain ratio governs modulus tuning over time, the macroscopic strain variation in Eq. (15) will be fixed to the parameter set $\mathcal{P}^\epsilon$, as follows:

$$\mathcal{P}^\epsilon : \{m_{ij}^\epsilon, a_{ij}^\epsilon, T_{ij}^\epsilon\} = \{0.035, 0.01, T_o\} \tag{20}$$

This set will be employed only for the active components of $\bar{\boldsymbol{\epsilon}}$ and always with $T_o = 1.8$ s (undenoted components are inactive and zero). The macroscopic stress variation, on the other hand, will be varied among the examples to explore the capabilities and limits of optimization. Only the indicated stress components will be incorporated into the tracking error, Eq. (17). Presently, $\bar{\epsilon}_{11}$ will be active and $\bar{\sigma}_{11}^*$ in Eq. (16) is targeted with the parameter set $\mathcal{P}_{\cos}^\sigma$, as follows:

$$\mathcal{P}_{\cos}^\sigma : \{\text{cyc}, m_{11}^\sigma, a_{11}^\sigma, T_{11}^\sigma, \theta_{11}\} = \{\cos, 0.8\,\text{MPa}, 0.16\,\text{MPa}, T_o, 0\} \tag{21}$$

Only the second phase of the microstructure is tunable based on Eq. (14) parameters and the volume fraction $\{E^{(1)}, E_o^{(2)}, \rho^*\} = \{3.6\,\text{MPa}, 108\,\text{MPa}, 0.45\}$. The stress in tunable materials can easily be varied by fifty percent (Jackson et al., 2018; Li et al., 2014; Shan et al., 2015; Zhang et al., 2018). Therefore, the amplitude of the variable modulus will always be set to $\Delta E^{(\alpha)} = E_o^{(2)}/2$ for simplicity without loss of generality in view of the given flexibility in choosing $\bar{\boldsymbol{\sigma}}^*(t)$. The number of time steps in time optimization will be chosen as $N_t = 18$ (Section 3.2), delivering a time step size of 0.1 s.

Figure 6 displays the prescribed target elliptic path $\bar{\sigma}_{11}^*$ in the macroscopic stress–strain space along with the actual response $\bar{\sigma}_{11}$ that the chosen microstructure delivers through the adaption of the microscopic modulus $E^{(2)}(t)$ via $\tau^{(2)}$. In all temporal adaption figures, three periods are plotted for clarity. Clearly, the target macroscopic response is realizable with the given microscopic input. On the other hand, an alternative target path is prescribed in Fig. 7 via the parameter set $\mathcal{P}_{\text{saw}}^\sigma$, where tri stands for a distorted triangular pattern:

$$\mathcal{P}_{\text{tri}}^\sigma : \{\text{cyc}, m_{ij}^\sigma, a_{ij}^\sigma, T_{ij}^\sigma, \theta_{ij}\} = \{\text{tri}, 1.0\,\text{MPa}, 0.5\,\text{MPa}, 1.8\,\text{s}, -\pi/2\} \tag{22}$$

The peak of this variation is set at $T_o/5$, with $T_o/2$ corresponding to a perfect triangular pattern. This target path is observed to be unrealizable because $E^{(2)}(t)$ saturates to its maximum value $E_{\max}^{(2)}$ at portions of a period, inducing
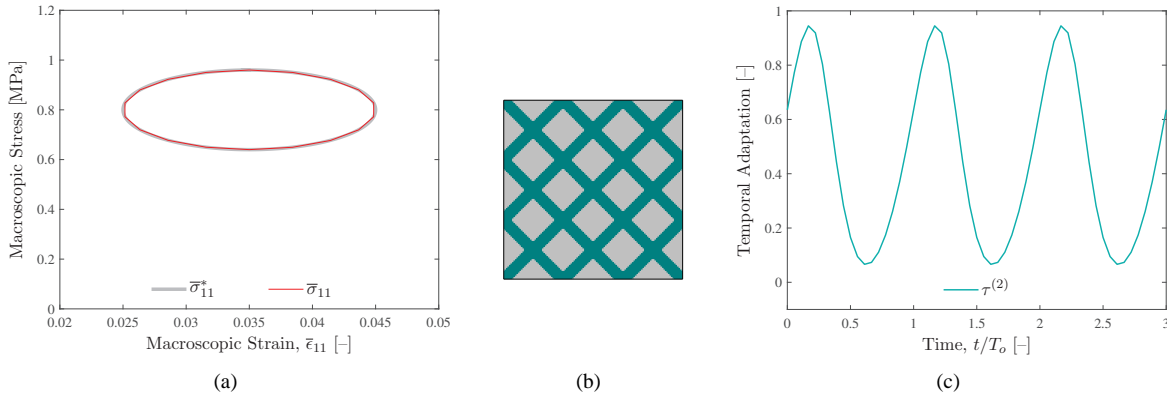
FIG. 6: Time optimization is carried out for a realizable target macroscopic stress–strain path [(a) macroscopic path, (b) unit cell, and (c) microscopic modulus], with a prescribed microstructure. In all temporal adaptation figures, three periods are plotted for clarity. In all macroscopic paths, the relevant strain component variation will follow Eq. (20). Presently, the target stress variation follows Eq. (21).
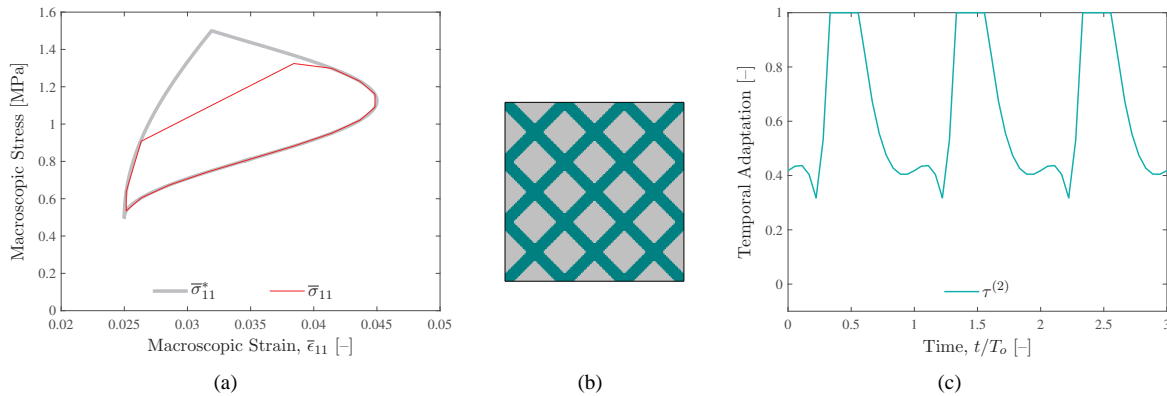

FIG. 7: Time optimization is carried out for an unrealizable target macroscopic stress–strain path [(a) macroscopic path, (b) unit cell, and (c) microscopic adaptation], with the prescribed microstructure of Fig. 6. Here, the target macroscopic stress variation follows Eq. (22).

similar maximum saturation in $\overline{\overline{\mathbb{E}}}$, yet this is not sufficient for successful tracking of the prescribed path (Özcan et al., 2020).

Although further flexibility can be assigned to the microstructure by setting $E_{\max}^{(2)}$ to a larger value, arbitrary flexibility in microscopic tunability may not be physically possible. Moreover, the appropriate choice of the limits depends on the target path and can always be insufficient, either through the maximum or minimum limit. Instead, Fig. 8 demonstrates that combined space–time optimization can realize the target path almost perfectly by adapting the microstructure topology and the unit cell domain within which this topology resides, without altering the physical properties. This highlights the additional flexibility of space–time topology optimization. Note that the spatial topology is time independent—it is optimized only to provide the optimal freedom for the development of the temporal topology.

The number of time steps chosen in time optimization does not influence the objective function significantly, because the objective can be driven toward zero whenever the target is realizable, which only requires a nearly vanishing error at each sampling point in time. However, the number of time steps does affect the visual quality of optimization. To demonstrate its influence, the analysis of Fig. 8 is repeated by decreasing the number of time steps from its default value of $N_t = 18$ to $N_t = 9$. Despite the fact that this choice also delivers a satisfactory outcome, the visual quality is slightly inferior to the default choice (Fig. 9). On the other hand, the results with a higher time
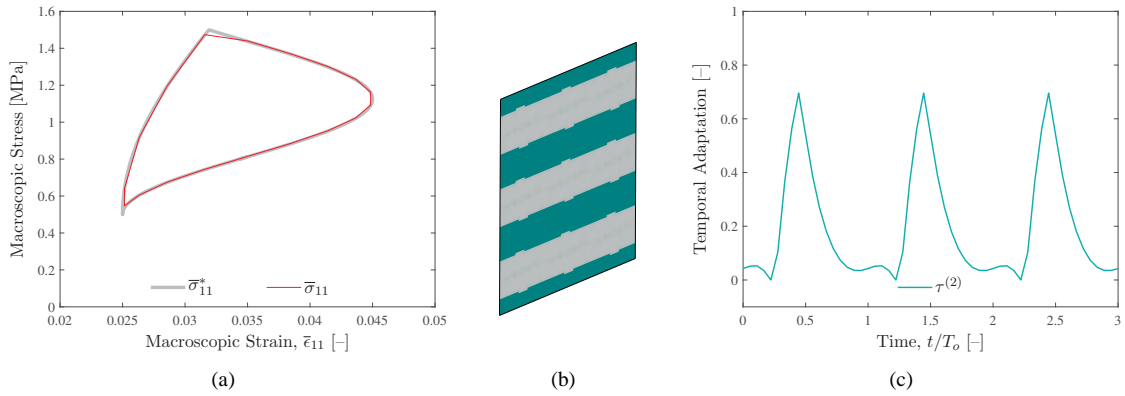
(a)   (b)   (c)

FIG. 8: Space–time optimization is carried out for the target macroscopic stress–strain path of Fig. 7: (a) macroscopic path, (b) unit cell, and (c) microscopic adaptation
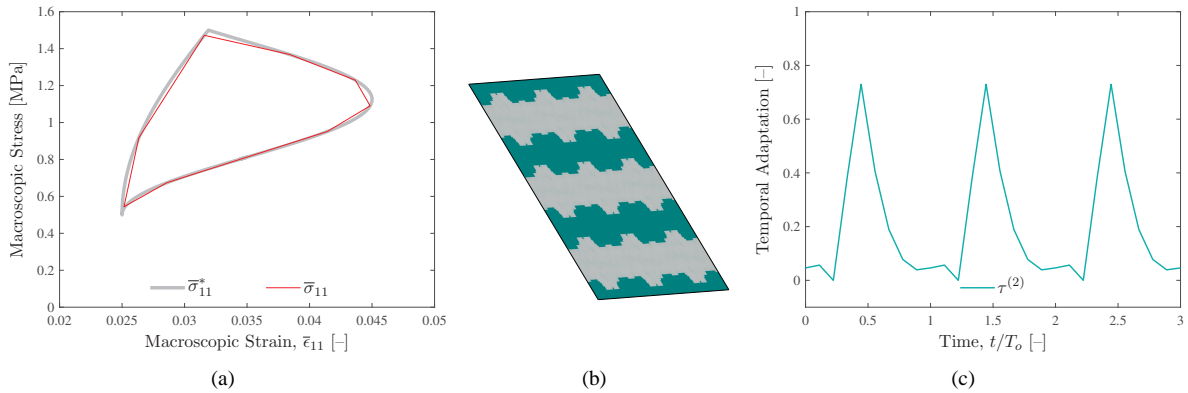

(a)   (b)   (c)

FIG. 9: The analysis in Fig. 8 is repeated by decreasing the number of time steps from its default value of $N_t = 18$ to $N_t = 9$: (a) macroscopic path, (b) unit cell, and (c) microscopic adaptation

resolution at $N_t = 27$ (not shown) are virtually identical to the results in Fig. 8. For all three cases, the objective error was $< 1\%$. Considering that the optimization time scales linearly with N_t, these observations justify the default choice as a time resolution, which delivers a satisfactory visual optimization quality at an acceptable computational cost.

4.3 Multiple Stress Targets

If only one microscopic phase is tunable and a single macroscopic path is targeted, this is highly achievable to within the limits of realizability. When perfect tracking is obtained, e.g., via $E^{(2)}(t)$ in the $\overline{\epsilon}_{11} - \overline{\sigma}_{11}$ space as in the preceding examples, the variation of the remaining macroscopic stress components are automatically induced through the relation $\overline{\boldsymbol{\sigma}}(t) = \overline{\overline{\mathbb{E}}}(t)\overline{\boldsymbol{\epsilon}}(t)$. Therefore, to have a thus far unmonitored macroscopic stress component to follow a target path that differs from this induced response can in general only be achieved by sacrificing from the quality with which the original objective has been optimized. In such cases, an increasing number of microscopic tuning degrees of freedom enhances the number of macroscopic stress–strain paths that can be successfully tracked. In order to demonstrate this feature, biaxial deformation is applied on a unit cell via ϵ_{11} and ϵ_{22} components, both varying according to Eq. (20) as noted earlier, with all other strain components set to zero. The target for $\overline{\sigma}_{22}$ is based on the sinusoidal variation [Eq. (21)] with updated values. Note that this variation effectively differs from the strain variation [Eq. (20)] through a phase, thereby causing a closed loop (Özcan et al., 2020). For $\overline{\sigma}_{11}$, a doubly oscillatory sinusoidal target signal is chosen, which also differs through its period, thereby causing the macroscopic stress–strain loop to cross itself, as follows:

$$\mathcal{P}_{\text{dos}}^{\sigma} : \{\text{cyc}, m_{11}^{\sigma}, a_{11}^{\sigma}, T_{11}^{\sigma}, \theta_{11}\} = \{\sin, 1.4\,\text{MPa}, 0.14\,\text{MPa}, T_o/2, 0\} \tag{23}$$

Both phases are active based on the parameters $\{E_o^{(1)}, E_o^{(2)}, \rho^*\} = \{18\,\text{MPa}, 108\,\text{MPa}, 0.5\}$, with $\Delta E^{(\alpha)} = E_o^{(\alpha)}/2$ as the default choice. The result of the space–time optimization is summarized in Fig. 10. Because only one of the target stresses have a period that is half of the strain period, it would not be possible to achieve successful tracking of both paths unless both phases are tunable. It is highlighted that the macroscopic stress variations are always described with respect to time—the paths with respect to the corresponding strain components are displayed as a graphical assessment of the optimization quality.

The target paths are not limited to normal stresses. As an example, $\overline{\sigma}_{22}^*$ is set according to Eq. (23) while $\overline{\sigma}_{12}^*$ follows Eq. (22). Figure 11 summarizes the successful space–time optimization result. It is noted that the presence of two tunable phases does not guarantee that two arbitrary macroscopic stress–strain paths can be tracked successfully.

Multiple stress targets are additionally employed within a three-dimensional setting in Figs. 12 and 13, where $N_m = 30$ is employed again. For the microstructure in Fig. 13(a), pure time optimization is first carried out based on realizable target paths that are described through two shear stress components. The results in Fig. 12(a) indicate successful optimization, but the oscillations in one of the signals also point to a possible need to employ filtering of the temporal design variables as an exception to the choice adopted in this work, cf. Section 3.2. Subsequently, the target paths are modified in Fig. 12(b) such that pure time optimization on the same fixed microstructure is no longer sufficient for successful tracking. However, when combined space–time optimization is involved, the same targets can be successfully attained in Fig. 12(c) with the corresponding microstructure in Fig. 13(b), which has formed within a domain geometry that is significantly rotated and stretched with respect to the original cubic one.
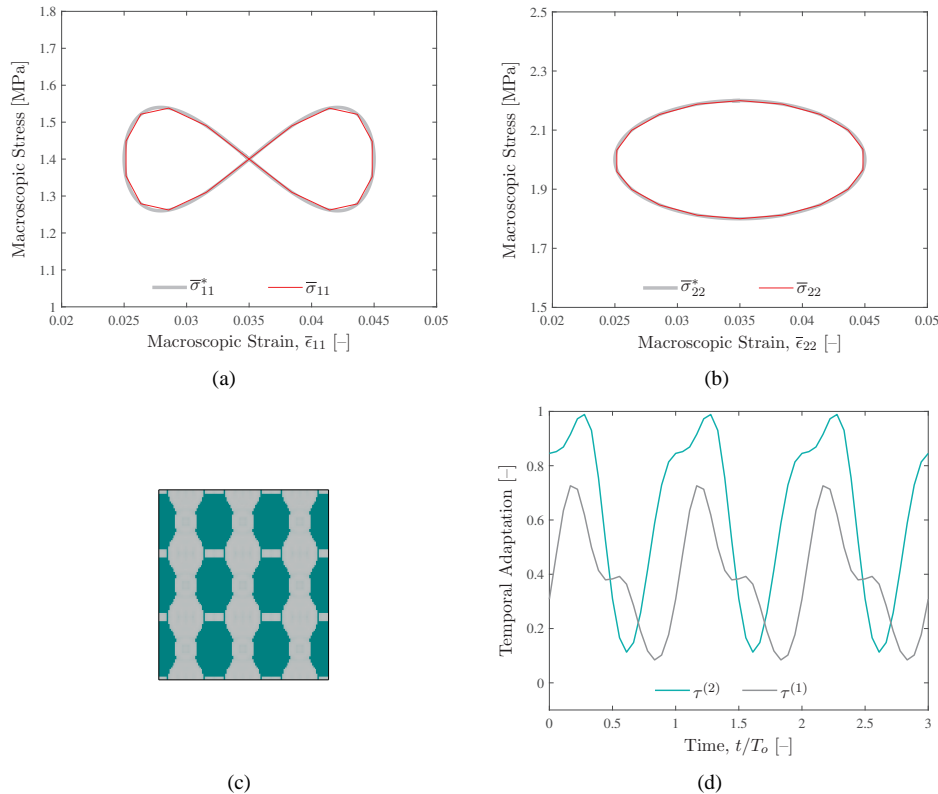

(a)

(b)

(c)

(d)

FIG. 10: Space–time optimization is carried out toward the simultaneous realization of the depicted target normal stress paths: (a) macroscopic path – normal 1, (b) macroscopic path – normal 2, (c) unit cell, and (d) microscopic adaptation. Similar to the phases in the microstructure, the lines are associated with $E^{(1)}(t)$ and $E^{(2)}(t)$, respectively. Here, $\overline{\sigma}_{11}^*$ is described via Eq. (23) whereas $\overline{\sigma}_{22}^*$ follows Eq. (21) with updated values $\{m_{22}^{\sigma}, a_{22}^{\sigma}\} = \{2.0\,\text{MPa}, 0.2\,\text{MPa}\}$. Refer to the online version for color.
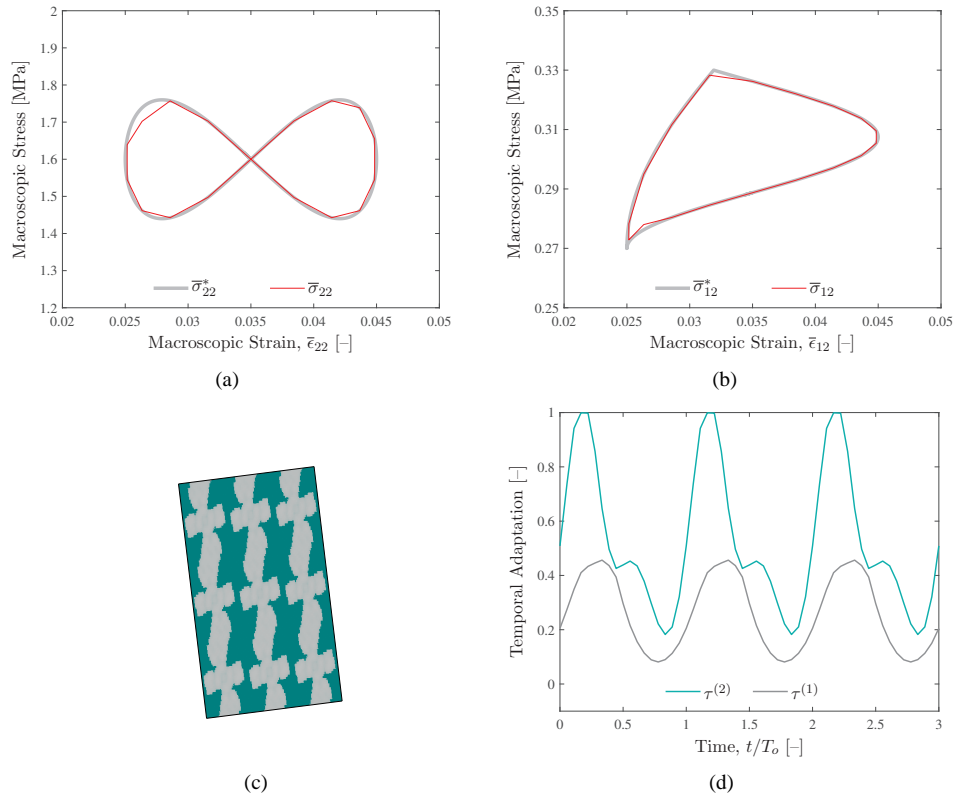
(a)

(b)

(c)

(d)

FIG. 11: Space–time optimization is carried out under a combination of normal and shear target stresses: (a) macroscopic path – normal, (b) macroscopic path – shear, (c) unit cell, and (d) microscopic adaptation. Here, $\overline{\sigma}_{22}^*$ is described via Eq. (23), with updated values $\{m_{22}^\sigma, a_{22}^\sigma\} = \{1.6\,\text{MPa}, 0.16\,\text{MPa}\}$ while $\overline{\sigma}_{12}^*$ follows Eq. (22) with the values $\{m_{12}^\sigma, a_{12}^\sigma\} = \{0.3\,\text{MPa}, 0.03\,\text{MPa}\}$.

4.4 Unrealizable Cases

The purpose of this section is to discuss possible deterioration in optimization quality when the number of target stresses exceeds the number of tunable phases, as alluded to in Section 4.3. As a particular example, the setting of Fig. 10 is revisited with one difference, $\overline{\epsilon}_{12}$ now also varies according to the default parameter set [Eq. (20)], which induces a new unit cell loading. As a consequence, even when $\overline{\sigma}_{12}$ is not monitored as a target within Eq. (17), the optimization result must differ from Fig. 10 where $\overline{\epsilon}_{12} = 0$, which is observed in Figs. 14(a) and 15(a). Within Fig. 14(a), the unmonitored induced shear stress $\overline{\sigma}_{12}^o(t)$ is also displayed. If optimization was carried out while taking into account this variation as a target, the problem remains trivially realizable and the same result is obtained.

If $\overline{\sigma}_{12}^*$ is modified to away from the induced response $\overline{\sigma}_{12}^o(t)$, for instance through a shift Δm_{12}^σ of the mean, then the mismatch between $\overline{\sigma}_{12}^* = \Delta m_{12}^\sigma + \overline{\sigma}_{12}^o(t)$ and $\overline{\sigma}_{12}^o(t)$ will force optimization to seek an alternative optimum. This is summarized in Figs. 14(b) and 15(b). Clearly, although the signals have not saturated and hence the performance is not restricted by the elastic moduli limits, the optimization problem is not realizable, i.e., it is not possible to track all three target macroscopic stress variations perfectly with two tunable microscopic phases. In this particular case, the degree of unrealizability can be controlled through the amount of shift of Δm_{12}^σ and will serve as a testbed to compare the space–time optimization approach with the control approach in Section 4.5. Introducing more than two tunable phases may increase the flexibility of the approach to decrease the optimization error or even render the problem realizable. However, this requires a multi-material topology optimization framework that is beyond the scope of the present study. In any case, the significant advantage of space–time optimization is additionally demonstrated in Fig. 14(c), where it is observed that time optimization alone, based on the initial microstructure from Fig. 15(a), delivers a response that remains comparatively inferior to a significant extent.
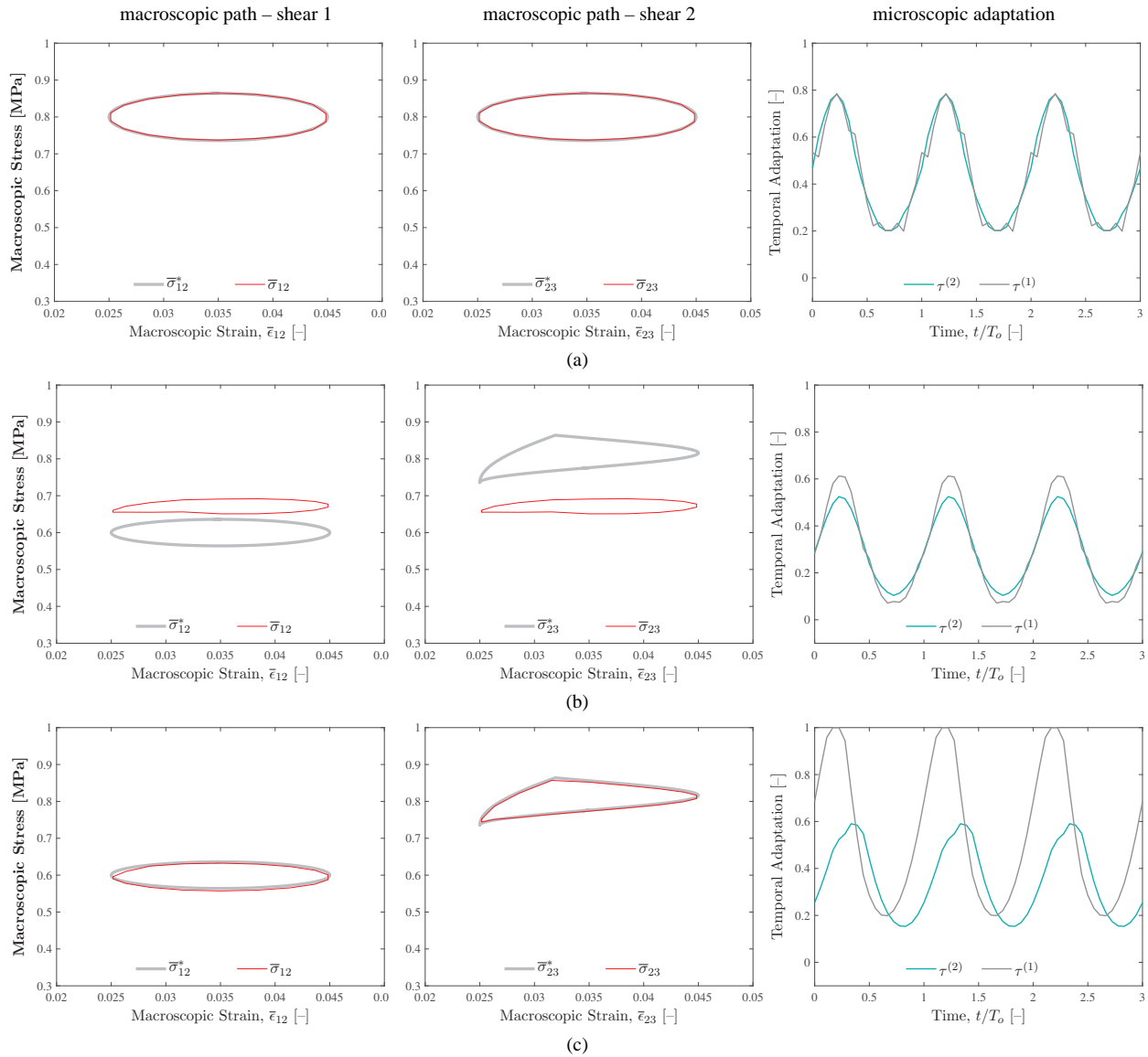
FIG. 12: Three-dimensional optimization results are summarized, with the corresponding microstructures in Fig. 13. Cases (a) and (b) correspond to pure time optimization, the latter appearing unrealizable due to a fixed microstructure. Combined space–time topology optimization in case (c) demonstrates that the target paths are in fact realizable. For case (a), both target paths are described through Eq. (21) except that the amplitude is set to 0.08. For cases (b) and (c), the first path is again similar with the mean reduced to 0.6 and the amplitude to 0.06. The second path follows Eq. (22) with the mean and amplitude chosen as for (a).

4.5 Control Approach to Optimization in Time

The space–time topology optimization framework delivers an optimal microstructure for a target macroscopic stress–strain path. The practical implementation of a material with this tunable microstructure requires a control framework (Ogata and Yang, 2002), where an actuator applies deformation to the material to induce a desired strain and the microstructure is continuously tuned such that the stress state that is measured by the sensor follows the desired variation, essentially corresponding to time optimization via the tuning signals $\tau^{(\alpha)}(t)$. In an ideal setting, an open-loop control implementation may be pursued where the microstructure follows the tuning path via $\tau^{(\alpha)}(t)$, which is
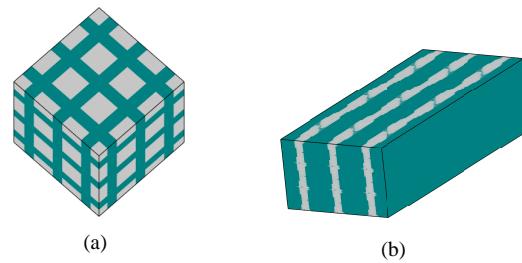
<div align="center">(a)   (b)</div>

FIG. 13: The microstructure in (a) fixed unit cell, is employed in cases (a) and (b) of Fig. 12 as a prescribed input. The microstructure in (b) optimized unit cell, where the gray phase is nearly uniform along the vertical direction, is obtained through combined space–time optimization that is associated with case (c) of Fig. 12. Both microstructures are based on $\{E_o^{(1)}, E_o^{(2)}, \rho^*\} = \{18\,\text{MPa}, 108\,\text{MPa}, 0.7\}$.

determined through the present framework in order to trace the macroscopic path successfully. In practice, however, deviations from this ideal path are expected due to real-life aspects of implementation, such as delay in sensing and actuation. As a consequence, $\tau^{(\alpha)}(t)$ must be updated on the fly accordingly in order to ensure minimal tracking error. The practical realization of this update crucially relies on a closed-loop feedback control framework. Pure time optimization, as in the example of Fig. 6, cannot be employed because a deviation (such as delay) is not known *a priori*. In this section, the implementation of time optimization through such a control structure and its performance in the presence of common practical application issues will be very briefly discussed. Although a control approach is motivated by practical considerations, the focus will be on the closed-loop feedback structure without important practical ingredients, such as actuator models or controller communication delays [see Özcan et al. (2020), for examples].

The feedback controller employed in the present implementation is a multiple-input–multiple output repetitive controller operated to regulate the behavior of the tunable material model (Fig. 16). The repetitive controller structure is an algorithm developed based on the internal model principle (Francis and Wonham, 1975). It aims to achieve a zero steady-state error by repeating the input characteristics through a specific structure with a time delay inside the control algorithm. It produces superior steady-state error performance for systems with fixed periodic reference inputs and is easy to implement in realistic applications (Wang et al., 2009). The structure employed in this work is based on Hara et al. (1988) and adapted toward the smart composite material system. This structure was chosen as the control method for $\tau^{(\alpha)}$ in Özcan et al. (2020). Presently, it will be employed to further assess the optimality of the present framework with respect to the temporal dimension. Additionally, the efficiency of this approach will be further improved through a database approach to homogenization.

In Fig. 16, $C(S)$ represents the unified control algorithm. It consists of a proportional gain controller with a multiplicative constant, P, and a repetitive block structure. The repetitive block structure utilizes the one-period delay error value (calculated using the transport delay element, $e^{-\tau s}$) with the current value of the error signal to eliminate the steady-state error for repeating input signals. At every cycle, the controller takes the value of the $\tau^{(\alpha)}$ signals from the cycle before and updates the controller output calculated using the current error signal. The repetitive control structure gives the control system a simple but effective adjusting ability since it utilizes the repeating information it has acquired from the earlier cycles.

A critical ingredient of the controller is an inverse material model algorithm that generates a rapid and computationally efficient signal compensation for the controller input so that the transient properties of the feedback controller are improved. Specifically, in order to simulate the response of the smart material for controller development and validation purposes, the cell problem [Eq. (3)] needs to be solved at every time step, similar to the pure time optimization setting of Fig. 6. This computationally expensive process may slow down the controller development and validation for rapid deployment and maintenance. In order to overcome this computational load, a material model has been developed through a temporal database—essentially a lookup table that contains the solutions of the cell problem and the resulting components of $\overline{\mathbb{E}}$ in the $\tau^{(1)} - \tau^{(2)}$ space with a resolution of 0.025 along each axis. When the tuning signals $\tau^{(\alpha)}$ fall within data points of the lookup table, bilinear interpolation is employed. Although the details will not be provided, this approach also facilitates the development of the inverse material model that is needed for the
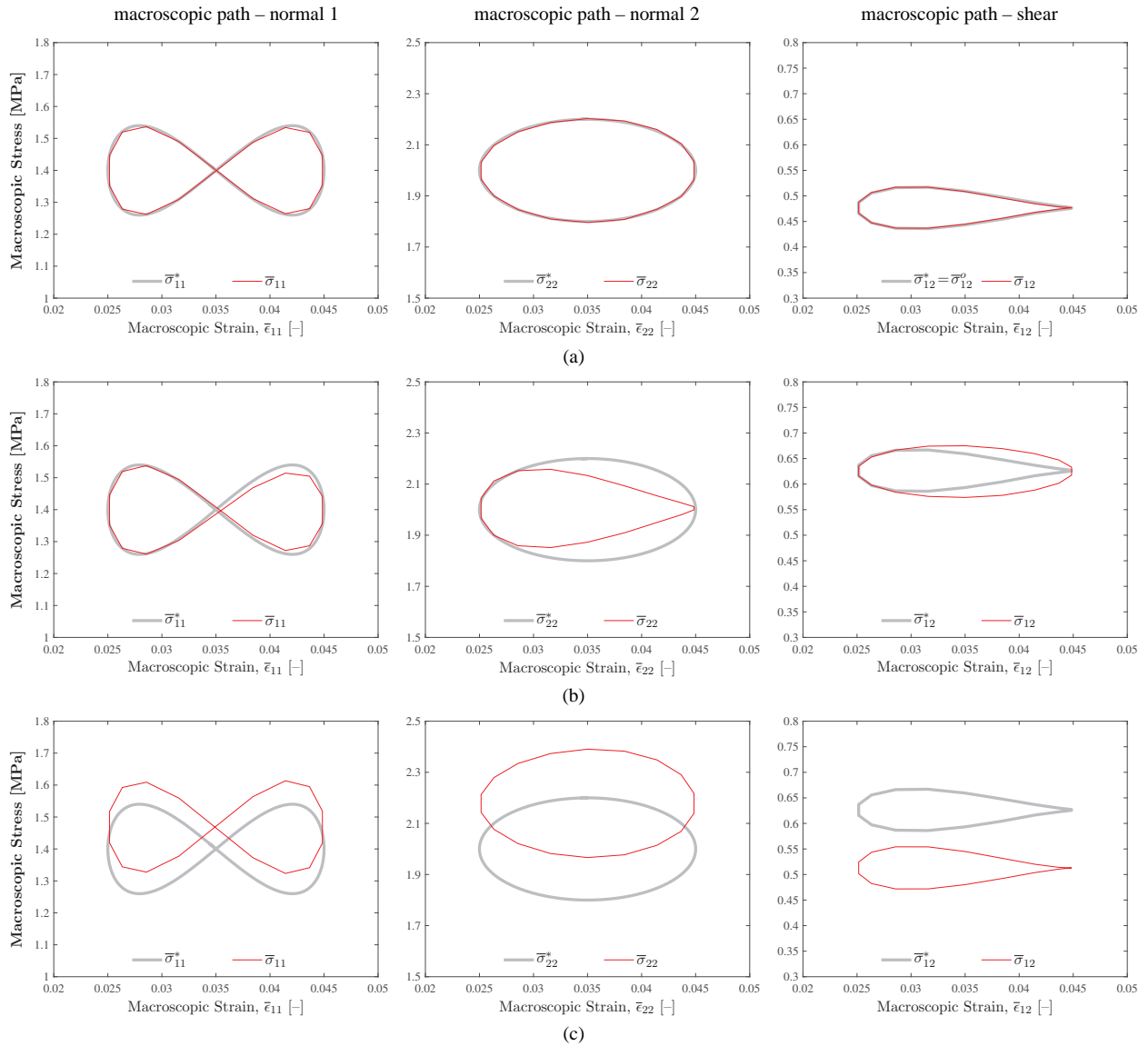
FIG. 14: In case (a), the space–time optimization is carried out for the setting of Fig. 10 by additionally setting $\overline{\epsilon}_{12}$ to vary according to Eq. (20) and setting the target for $\overline{\sigma}_{12}$ as the induced response $\overline{\sigma}_{12}^o(t)$. In case (b), this target is modified through a change of mean as $\overline{\sigma}_{12}^* = \Delta m_{12}^\sigma + \overline{\sigma}_{12}^o(t)$, which renders the problem unrealizable. The corresponding space–time topologies are summarized in Fig. 15. In case (c), only time optimization is carried out for the target of case (b) based on the initial microstructure from case (a).

controller, essentially to predict the amount of update to the tuning signals that are needed in order to derive the tracking error to a minimum.

In order to demonstrate the control algorithm, the example of Fig. 6 is now revisited in Fig. 17 with the same microstructure. Unlike the earlier topology optimization framework, the control approach delivers a variation that is updated through each period toward the target macroscopic stress–strain path. After less than ten periods, the tracking error already decreases significantly and continues to monotonically decrease toward a perfect match of the actual and target paths. Whenever the target is realizable, the control algorithm systematically diminishes the error. In order to analyze its performance in an unrealizable setting, the example of Section 4.4 is revisited where the macroscopic
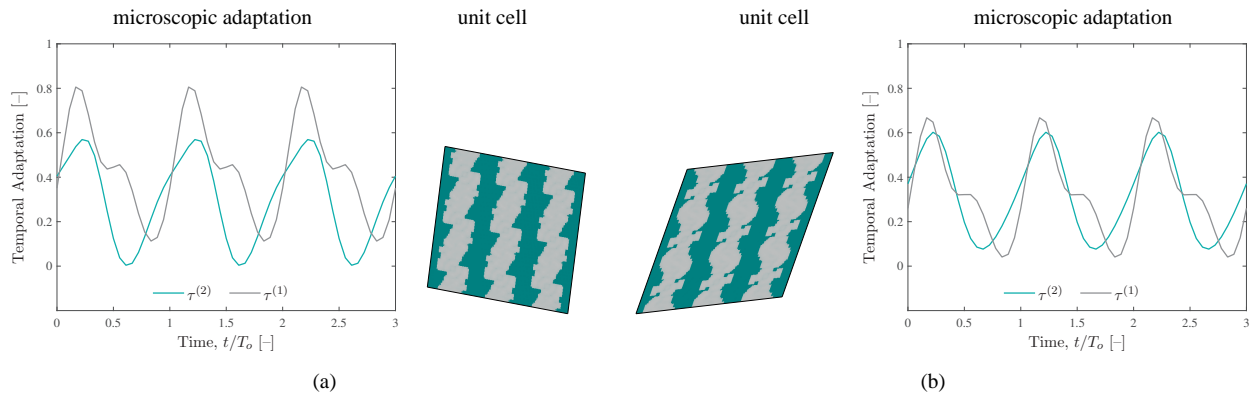
(a)

(b)

FIG. 15: Space–time topologies corresponding to cases (a) and (b) of Fig. 14 are summarized
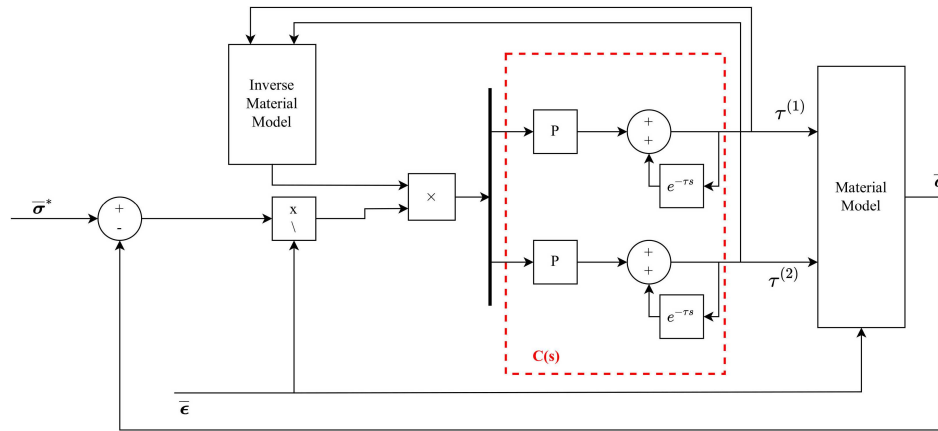

FIG. 16: Proposed system for controlling the tuning signals $\tau^{(\alpha)}$

shear stress target is altered through a mean shift, presently chosen as $\Delta m_{12}^{\sigma} = 0.05\alpha$, where α will control the degree of unrealizability. The tracking error for varying degrees is summarized in Fig. 18.

When $\alpha = 0$, the realizable setting of Fig. 14 is recovered and zero tracking error can be achieved for all approaches. As the degree of unrealizability is increased, pure time optimization on the fixed microstructure that was obtained at $\alpha = 0$ delivers a monotonically increasing error. Minimization of the tracking error has not been embedded into the design of the control algorithm as an objective directly. Therefore, it delivers a time adaptation that remains slightly inferior with respect to time optimization. Nevertheless, because the controller attempts to minimize the pointwise error in the macroscopic stress over the period, the results from the two approaches remain close. From a practical perspective, this indicates that the performance obtained through the controller in the implementation of the tunable microstructure will remain close to optimal. Finally, the remarkably lower error associated with combined space–time topology optimization is additionally displayed. Such an error curve could conceivably be followed by a microstructure where not only the constitutive parameters but also the spatial topology can be adapted over time. Such spatial topology adaptation appears to have been rendered feasible very recently for surfaces (Visschers et al., 2021) but continues to remain challenging for materials.

5. CONCLUSION

Smart materials respond to external stimuli such as thermal and magnetic fields in a continuous and controllable manner, resulting in an observable change in their mechanical response. The microstructure of such materials plays a
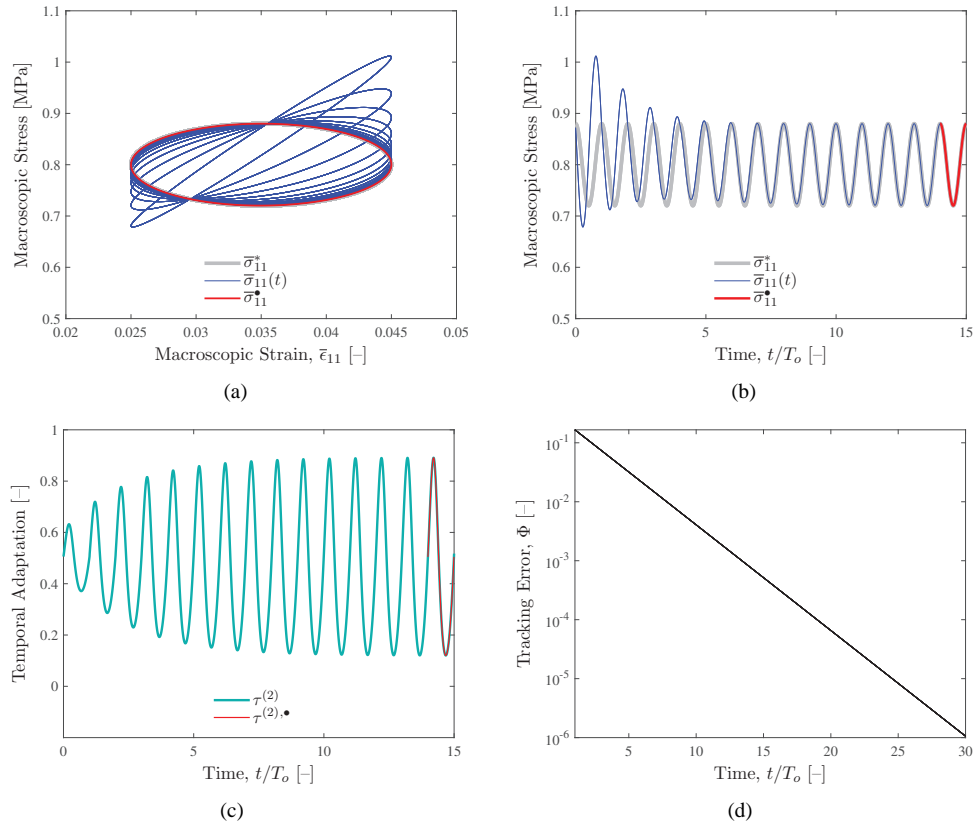
(a)

(b)

(c)

(d)

FIG. 17: The controller performance is demonstrated for the time optimization example of Fig. 6. Here, the initial value of the tunable modulus is prescribed as the mean value $E^{(2)}(0) = E_o^{(2)}$. The notation $()^\bullet$ highlights the response through the 15th cycle for comparison with the earlier time optimization result: (a) macroscopic path, (b) macroscopic stress, (c) microscopic adaptation, and (d) tracking error.
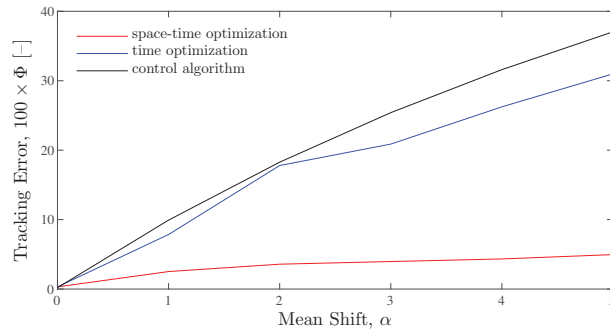

FIG. 18: The adaptation performance of the three different approaches when $\overline{\sigma}_{12}^* = \Delta m_{12}^\sigma + \overline{\sigma}_{12}^o(t)$ is employed with $\Delta m_{12}^\sigma = 0.05\alpha$ in the setting of Fig. 14

fundamental role in delivering the desired level and nature of macroscopic tunability. Earlier studies have investigated the link between the microstructural geometry and the macroscopic tunability in experimental and numerical settings. In the present work, a topology optimization framework is developed in order to design the microstructure so as to offer maximum flexibility in tuning in order to attain the desired macroscopic time-dependent response. This framework treats temporal design variables that are associated with the external stimuli and spatial design variables that

associated with the microscopic material distribution on an equal footing. The incorporation of the geometry within which the material distribution is sought into the design framework endows further flexibility toward minimizing the optimization error.

A range of numerical investigations have demonstrated the viability of the approach to capture an optimal design for both realizable as well as unrealizable target cyclic paths in the stress–strain space. The overall methodology constitutes a viable design framework for extension along a number of directions. It is conceivable that the degree of unrealizability depends on the number of tunable microscopic constituents, which can be investigated within a multimaterial optimization framework. Additionally, a model for the constitutive link between the external stimuli and the tuning response can help assess the limits and dynamics of tunability in realistic scenarios.

Finally, a degree of programmability in the microscopic geometry can be incorporated into the design framework in addition to stimulus-sensitive phases for improved adaptation to time-dependent demands. Such extensions will contribute to the efforts toward the design and analysis of smart materials, which can successfully attain objectives where traditional materials fail to perform optimally.

REFERENCES

Ansari, M.H., Attarzadeh, M.A., Nouh, M., and Karami, M.A., Application of Magnetoelastic Materials in Spatiotemporally Modulated Phononic Crystals for Nonreciprocal Wave Propagation, *Smart Mater. Struc.*, vol. **27**, p. 015030, 2018.

Ashcroft, N.W. and Mermin, N.D., *Solid State Physics*, Boston: Cengage, 1976.

Barbarosie, C. and Toader, A.M., Optimization of Bodies with Locally Periodic Microstructure by Varying the Periodicity Pattern, *Netw. Heterog. Media*, vol. **9**, pp. 433–451, 2014.

Bendsøe, M.P. and Sigmund, O., *Topology Optimization: Theory, Methods and Applications*, 2nd ed., New York: Springer, 2004.

Bensøe, M.P. and Kikuchi, N., Generating Optimal Toplogies in Structural Design Using a Homogenization Method, *Comput. Methods Appl. Mech. Eng.*, vol. **71**, pp. 197–224, 1988.

Bou Matar, O., Robillard, J.F., Vasseur, J.O., Hladky-Hennion, A.C., Deymier, P.A., Pernod, P., and Preobrazhensky, V., Band Gap Tunability of Magneto-Elastic Phononic Crystal, *J. Appl. Phys.*, vol. **111**, no. 5, p. 054901, 2012.

Cai, P., Wang, C., Gao, H., and Chen, X., Mechanomaterials: A Rational Deployment of Forces and Geometries in Programming Functional Materials, *Adv. Mater.*, vol. **33**, p. 2007977, 2021.

Çakal, B.A., Temizer, I., Terada, K., and Kato, J., Microscopic Design and Optimization of Hydrodynamically Lubricated Dissipative Interfaces, *Int. J. Numer. Methods Eng.*, vol. **120**, pp. 153–178, 2019.

Clausen, A., Wang, F., Jensen, J.S., Sigmund, O., and Lewis, J.A., Topology Optimized Architectures with Programmable Poisson's Ratio over Large Deformations, *Adv. Mater.*, vol. **27**, pp. 5523–5527, 2015.

Francis, B. and Wonham, W., The Internal Model Principle of Linear Control Theory, *IFAC Proc. Vol.*, vol. **8**, no. 1, pp. 331–336, 1975.

Gump, J., Finkler, I., Xia, H., Sooryakumar, R., Bresser, W.J., and Boolchand, P., Light-Induced Giant Softening of Network Glasses Observed near the Mean-Field Rigidity Transition, *Phys. Rev. Lett.*, vol. **92**, p. 245501, 2004.

Haghpanah, B., Ebrahimi, H., Mousanezhad, D., Hopkins, J., and Vaziri, A., Programmable Elastic Metamaterials, *Adv. Eng. Mater.*, vol. **18**, pp. 643–649, 2016a.

Haghpanah, B., Salah-Sharif, L., Pourrajab, P., Hopkins, J., and Valdevit, L., Multistable Shape-Reconfigurable Architected Materials, *Adv. Mater.*, vol. **28**, pp. 7915–7920, 2016b.

Hara, S., Yamamoto, Y., Omata, T., and Nakano, M., Repetitive Control System: A New Type Servo System for Periodic Exogenous Signals, *IEEE Trans. Autom. Control*, vol. **33**, no. 7, pp. 659–668, 1988.

Jackson, J.A., Messner, M.C., Dudukovic, N.A., Smith, W.L., Bekker, L., Moran, B., Golobic, A.M., Pascall, A.J., Duoss, E.B., Loh, K.J., and Spadaccini, C.M., Field Responsive Mechanical Metamaterials, *Sci. Adv.*, vol. **4**, p. eaau6419, 2018.

Kallio, M., Lindroos, T., Aalto, S., Järvinen, E., Kärnä, T., and Meinander, T., Dynamic Compression Testing of a Tunable Spring Element Consisting of a Magnetorheological Elastomer, *Smart Mater. Struct.*, vol. **16**, pp. 506–514, 2007.

Kuder, I.K., Arrieta, A.F., Raither, W.E., and Ermanni, P., Variable Stiffness Material and Structural Concepts for Morphing Applications, *Prog. Aerosp. Sci.*, vol. **63**, pp. 33–55, 2013.

Lee, J.H., Singer, J.P., and Thomas, E.L., Micro-/Nanostructured Mechanical Metamaterials, *Adv. Mater.*, vol. **24**, pp. 4782–4810, 2012.

Li, W.H., Zhou, Y., and Tian, T.F., Viscoelastic Properties of MR Elastomers under Harmonic Loading, *Rheol. Acta*, vol. **49**, pp. 733–740, 2010.

Li, Y., Li, J., Li, W., and Du, H., A State-of-the-Art Review on Magnetorheological Elastomer Devices, *Smart Mater. Struct.*, vol. **23**, p. 123001, 2014.

Liu, J., Gaynor, A.T., Chen, S., Kang, Z., Suresh, K., Takezawa, A., Li, L., Kato, J., Tang, J., Wang, C.C.L., Cheng, L., Liang, X., and To, A.C., Current and Future Trends in Topology Optimization for Additive Manufacturing, *Struct. Multidiscip. Optim.*, vol. **57**, p. 2457–2483, 2018.

Ogata, K. and Yang, Y., *Modern Control Engineering*, 4th ed., New York: Prentice Hall, 2002.

Özcan, M., Cakmakci, M., and Temizer, I., Smart Composites with Tunable Stress-Strain Curves, *Comput. Mech.*, vol. **65**, pp. 375–394, 2020.

Palacios, J., Calderin, L., Chon, A., Frankel, I., Alqasimi, J., Allein, F., Gorelik, R., Lata, T., Curradi, R., Lambert-Milak, G., Oke, A., Smith, N., Abi Ghanem, M., Lucas, P., Boechler, N., and Deymier, P., Temperature-Controlled Spatiotemporally Modulated Phononic Crystal for Achieving Nonreciprocal Acoustic Wave Propagation, *J. Acoust. Soc. America*, vol. **151**, pp. 3669–3675, 2022.

Rafsanjani, A., Akbarzadeh, A., and Pasini, D., Snapping Mechanical Metamaterials under Tension, *Adv. Mater.*, vol. **27**, pp. 5931–5935, 2015.

Restrepo, D., Mankame, N.D., and Zavattieri, P.D., Programmable Materials Based on Periodic Cellular Solids. Part I: Experiments, *Int. J. Solids Struct.*, vols. **100–101**, pp. 485–504, 2016a.

Restrepo, D., Mankame, N.D., and Zavattieri, P.D., Programmable Materials Based on Periodic Cellular Solids. Part II: Numerical Analysis, *Int. J. Solids Struct.*, vols. **100–101**, pp. 505–522, 2016b.

Sanchez-Palencia, E., *Non-Homogeneous Media and Vibration Theory*, Berlin: Springer-Verlag, 1980.

Shan, W., Diller, S., Tutcuoglu, A., and Majidi, C., Rigidity-Tuning Conductive Elastomer, *Smart Mater. Struct.*, vol. **24**, p. 065001, 2015.

Svanberg, K., The Method of Moving Asymptotes: A New Method for Structural Optimization, *Int. J. Numer. Methods Eng.*, vol. **24**, pp. 359–373, 1987.

Svanberg, K. and Svärd, H., Density Filters for Topology Optimization Based on the Pythagorean Means, *Struct. Multidisc. Optim.*, vol. **48**, pp. 859–875, 2013.

Trainiti, G., Xia, Y., Marconi, J., Cazzulani, G., Erturk, A., and Ruzzene, M., Time-Periodic Stiffness Modulation in Elastic Metamaterials for Selective Wave Filtering: Theory and Experiment, *Phys. Rev. Lett.*, vol. **122**, p. 124301, 2019.

Visschers, F.L.L., Broer, D.J., and Liu, D., Programmed Topographical Features Generated on Command in Confined Electroactive Films, *Soft Matter*, vol. **17**, pp. 7247–7251, 2021.

Wang, Y., Gao, F., and Doyle, F.J., Survey on Iterative Learning Control, Repetitive Control, and Run-to-Run Control, *J. Process Control*, vol. **19**, no. 10, pp. 1589–1600, 2009.

Wenz, F., Schmidt, I., Leichner, A., Lichti, T., Baumann, S., Andrae, H., and Eberl, C., Designing Shape Morphing Behavior through Local Programming of Mechanical Metamaterials, *Adv. Mater.*, vol. **33**, no. 37, p. 2008617, 2021.

Wu, J., Sigmund, O., and Groen, J.P., Topology Optimization of Multi-Scale Structures: A Review, *Struct. Multidiscip. Optim.*, vol. **63**, pp. 1455–1480, 2021.

Xia, X., Afshar, A., Yang, H., Portela, C.M., Kochmann, D.M., Di Leo, C.V., and Greer, J.R., Electrochemically Reconfigurable Architected Materials, *Nature*, vol. **573**, pp. 205–213, 2019.

Zhang, H., Guo, X., Wu, J., Fang, D., and Zhang, Y., Soft Mechanical Metamaterials with Unusual Swelling Behavior and Tunable Stress-strain Curves, *Sci. Adv.*, vol. **4**, no. 6, p. eaar8535, 2018.